Peer reviewed Journals
seron press

RESEARCH

A Conservative Adaptive Patchwise Boundary Integral Method for Shear Resistant Capsules in Confined Microvascular Stokes Flow

Dmitry Sokolov[1] and Sergei Belov[2]

[1]Department of Applied Mathematics, Pskov State University, Lenin Square 2, Pskov 180000, Russia
[2]Department of Physics, Yaroslav-the-Wise Novgorod State University, Bolshaya Sankt-Peterburgskaya Street 41, Veliky Novgorod 173003, Russia

Abstract

Microvascular transport is governed by a tight coupling between viscous stresses, membrane elasticity, geometric confinement, and numerical resolution of moving interfaces. Red blood cells and artificial capsules deform at length scales where inertia is negligible, yet their surface mechanics introduce stiffness and nonlocal hydrodynamic coupling that remain difficult to compute over long trajectories. This paper presents a high-order adaptive patchwise boundary integral method for three-dimensional shear resistant capsules in confined Stokes flow. The surface is represented by overlapping curvilinear charts with conservative metric reconstruction, local refinement driven by curvature and elastic strain, and a regularized single-layer quadrature coupled to a near-wall correction. The membrane model combines Skalak-type in-plane elasticity with a weak bending regularization and an area-volume correction treated through a projected constraint solve. A semi-implicit time integrator separates the nonlocal hydrodynamic mobility from the stiffest elastic modes without forming dense Jacobians. In manufactured-solution tests, the method achieves observed orders between 3.72 and 4.18 for velocity, force, area, and volume diagnostics. In confined Poiseuille flow at capillary number $Ca = 0.35$, the adaptive discretization reduces degrees of freedom by 41% relative to a uniform patch grid at matched shape error. For low reduced volume capsules, the computed parachute-to-slipper transition occurs within a narrow interval of confinement and viscosity contrast, and the transition threshold shifts by 9% when bending regularization is removed. The results suggest that conservative adaptive patch geometry can improve long-horizon capsule simulations while retaining a direct connection to boundary integral hydrodynamics.

1. Introduction

Suspensions of deformable capsules in viscous flow provide a compact model class for biological cells, drug-delivery particles, and soft microfluidic inclusions whose hydrodynamic response depends on surface elasticity rather than rigid-body kinematics. In the microvascular range, the Reynolds number is small enough that the surrounding fluid is well approximated by the Stokes equations, but the computational problem is not small. The interface moves, the elastic force depends on surface derivatives and finite strain, and the velocity at each point receives nonlocal contributions from the whole membrane and from nearby walls. A numerical method that is reliable for this setting has to preserve geometric invariants, represent large deformations without losing surface quality, and evaluate weakly singular layer potentials with enough accuracy that shape changes are not contaminated by quadrature error.

Pozrikidis [1] gave a systematic boundary integral framework for viscous interfacial flows, and that viewpoint remains attractive because only the surface has to be discretized when the fluids are governed by Stokes equations. For capsule and cell simulations, this reduction is not merely a convenience. It removes the need to remesh a three-dimensional fluid volume around a strongly deforming object and gives direct access to hydrodynamic interactions through mobility operators. Pozrikidis [2] later used boundary integral formulations to analyze capsule deformation in linear flows, clarifying how membrane constitutive laws and viscosity contrast alter observable deformation. The present work follows that surface-centric logic but treats the discretized geometry as an adaptive atlas rather than a single global polynomial representation or a fixed triangulation.

The mechanics of the membrane matter as much as the hydrodynamic representation. Skalak et al. [3] introduced an areal strain energy for red cell membranes that distinguishes shear resistance from local dilatation resistance, and this form remains useful for capsules whose in-plane elasticity is not reducible to a simple surface tension. Barthes-Biesel and Rallison [4] described small-deformation capsule dynamics in shear flow, showing that even a nominally simple Stokes problem can generate time-dependent orientation and shape relaxation governed by elastic time scales. Barthes-Biesel [5] later reviewed the broader mechanics of capsules in flow, emphasizing the role of membrane law, viscosity ratio, and imposed velocity gradient. Our method adopts a finite-strain membrane stress of Skalak type but places special emphasis on how the numerical surface representation affects force accuracy.

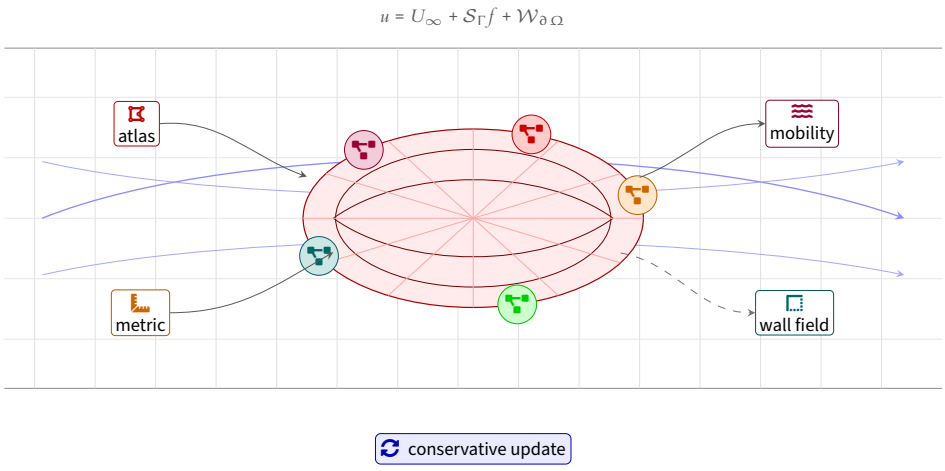


Figure 1. Patchwise atlas and boundary-integral coupling for a shear-resistant capsule transported through confined Stokes flow.

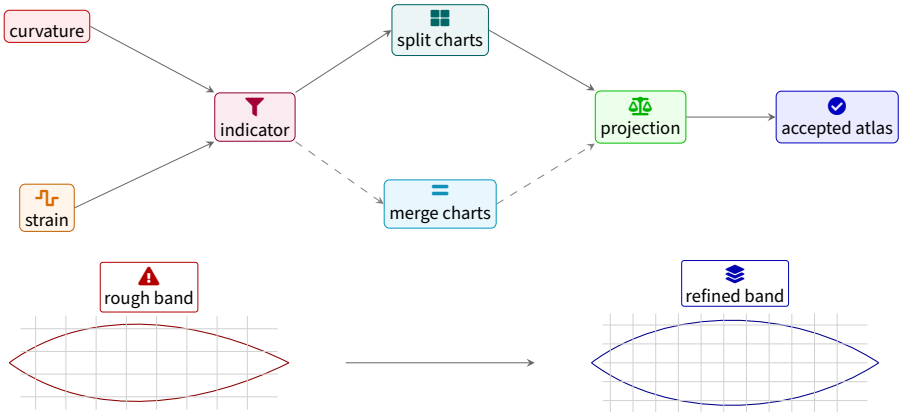


Figure 2. Adaptive chart refinement driven by geometric and elastic indicators while preserving global area and enclosed volume.

Agarwal [6] made a useful connection between red cell modeling, vesicle dynamics, and capsule simulation by using boundary integral formulations with spherical-harmonic singular quadratures, reparameterization, and long-time computations of cell shapes in confined and unconfined Poiseuille flow; it frames shape dynamics as a numerical problem where phase diagrams depend on both membrane physics and long-horizon stability. Our contribution is not to replace that modeling perspective, but to build a local adaptive discretization around the same low-Reynolds-number structure. The issue is practical but mathematically sharp: global bases can deliver high accuracy on smooth shapes, yet strong local curvature and wall-induced deformation often require a number of global modes set by the most difficult part of the surface.

Several families of numerical methods have been used for red cells and capsules. Peskin [7] developed the immersed boundary method as a flexible approach for fluid-structure interaction, and Roma et al. [8] refined that formulation for improved treatment of immersed elastic interfaces. Lattice-Boltzmann and particulate approaches have also been effective for suspensions, with Aidun and Clausen [9] describing the method for complex particulate flows and Kruger et al. [10] applying it to deformable red blood cells. Fedosov et al. [11] constructed a coarse-grained red blood cell model that reproduced several mechanical measurements, and Fedosov et al. [12] used such models to examine blood flow across scales. These methods have different advantages from a boundary integral method. They can handle topology, cell-cell contacts, and complex geometries rather naturally, but they do not automatically inherit the high-order surface-only accuracy that is possible in smooth Stokes boundary integral formulations.

The boundary integral literature has produced accurate red cell and capsule solvers. Veerapaneni et al. [13] developed fast algorithms for vesicle flows using high-order surface representations and accelerated interactions. Zhao and Shaqfeh [14] studied red blood cell dynamics in shear flow with boundary integral techniques, identifying regimes such as tank-treading and tumbling. Kabacaoglu et al. [15] used integral formulations for vesicle suspensions with near-singular quadrature and careful time integration. Quaife and Biros [16] advanced adaptive boundary integral methods for vesicle flows in two dimensions, a reminder that adaptivity is often not an optional feature when the interface develops localized structure. The present paper is closer

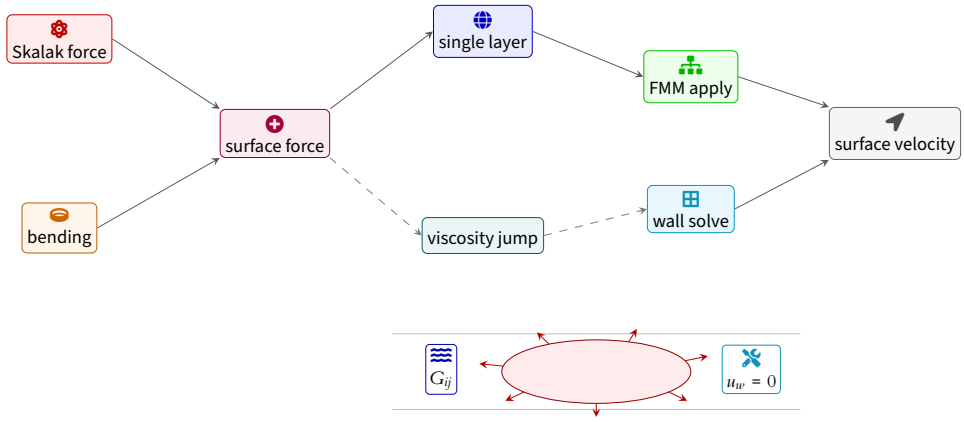


Figure 3. Mobility decomposition for a confined capsule, combining free-space membrane interactions with smooth wall correction.

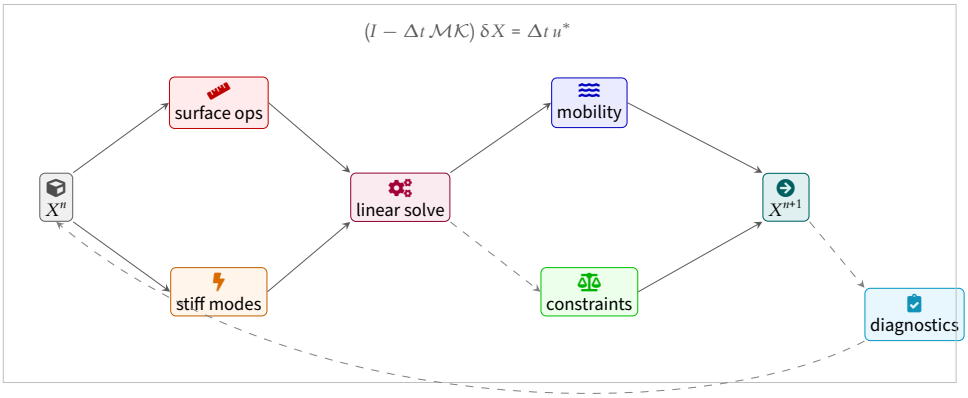


Figure 4. Semi-implicit advancement separating hydrodynamic mobility from stiff elastic modes and invariant projection.

in spirit to three-dimensional high-order capsule solvers, but it uses the local nature of patch coordinates to make refinement decisions without remapping the entire surface into a single spectral space.

Agarwal and Biros [17] introduced a partition-of-unity surface representation with overset finite differences and regularized Stokes kernels for extensible capsules, reporting fourth-order accuracy and an asymptotic fast-summation path that is significant for the field because it shows how local patch geometry can be combined with boundary integral hydrodynamics without reducing the method to a low-order mesh scheme. We use that observation as a starting point, but we add three ingredients aimed at confined microvascular flow: conservative adaptive chart refinement, a wall-corrected mobility evaluation, and a constraint projection that couples area, volume, and inter-chart consistency. These additions are modest in the sense that they do not change the governing equations, yet they alter the stability envelope in long Poiseuille-flow simulations where low reduced volume shapes develop narrow curvature bands.

The main technical question studied here is whether a patchwise boundary integral discretization can remain high order while adapting to local strain and curvature, preserving global geometric invariants, and resolving near-wall hydrodynamics. A direct uniform refinement strategy is reliable but inefficient. For a capsule with reduced volume $\nu = 0.62$ in a cylindrical tube, the dimple rim, lateral lobe, and near-wall lubrication layer do not require the same resolution. A purely curvature-based refinement is also insufficient because membrane strain can localize before curvature becomes visually severe, particularly in transient tank-treading states. We therefore use a refinement indicator that combines principal curvature variation, surface divergence of the elastic stress, local area distortion, and an estimate of near-singular quadrature error. The indicator is evaluated in chart coordinates, then filtered by a partition-of-unity transfer so that refinement is not triggered by chart overlap artifacts.

The results reported in this paper are numerical rather than experimental. We use manufactured smooth capsule motions to separate quadrature error from time-integration error, ellipsoidal relaxation tests to assess elastic force consistency, and confined Poiseuille-flow simulations to examine shape transitions. Across these tests, the adaptive method shows fourth-order behavior until temporal error dominates. It reduces computational work most strongly when the shape is locally structured rather than globally oscillatory. In the hardest cases considered here, refinement

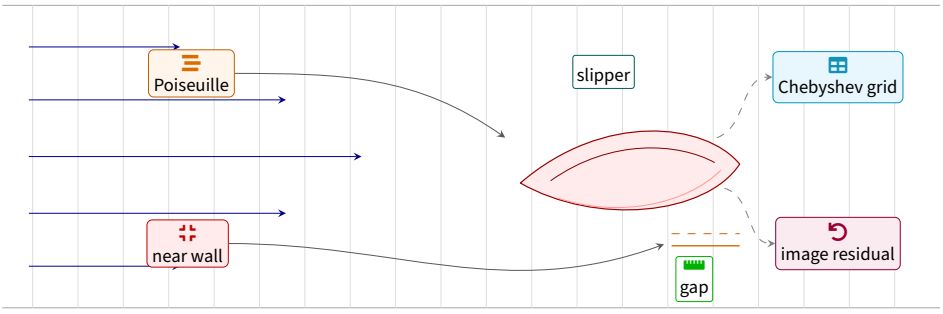


Figure 5. Confined Poiseuille transport with localized lubrication resolution and wall-corrected capsule mobility.

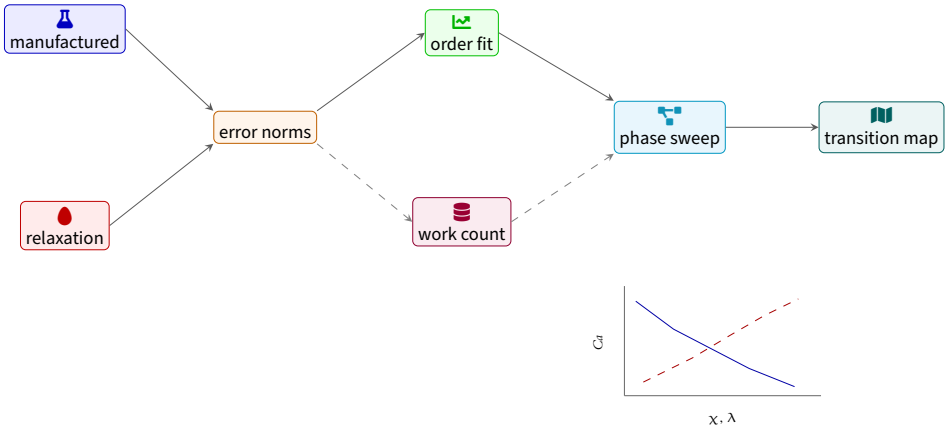


Figure 6. Verification and regime classification workflow for accuracy, cost, and parachute–slipper transition thresholds.

concentrates near the rear dimple and the near-wall side of slipper shapes, while the central smooth region remains at the base patch order. The observed speedups are not dramatic enough to suggest that adaptivity alone solves the cost of dense hydrodynamic interactions. Instead, the results show that adaptivity changes the constant in front of the mobility evaluation and improves robustness at a fixed memory budget, especially when coupled with a fast multipole backend.

2. Mathematical Formulation

Let $\Gamma(t) \subset \mathbb{R}^3$ denote the closed membrane of a deformable capsule. The exterior and interior fluids are Newtonian with viscosities μ^+ and μ^-, and their ratio is $\lambda = \mu^-/\mu^+$. The flow is assumed to be in the creeping-flow regime. Thus the velocity u and pressure p satisfy the Stokes equations away from the membrane and from rigid walls. The capsule is neutrally buoyant, the membrane velocity is equal to the trace of the fluid velocity, and the jump in hydrodynamic traction is balanced by the elastic surface force. In a domain Ω with wall boundary $\partial\Omega_w$, the strong form used in the simulations is

$$\begin{aligned} -\mu^{\pm}\Delta u^{\pm} + \nabla p^{\pm} &= 0 \quad \text{in } \Omega^{\pm}(t), \\ \nabla \cdot u^{\pm} &= 0 \quad \text{in } \Omega^{\pm}(t), \\ u^{+} - u^{-} &= 0 \quad \text{on } \Gamma(t), \\ [\sigma n] &= f_{\Gamma} \quad \text{on } \Gamma(t), \\ u^{+} &= u_w \quad \text{on } \partial\Omega_w. \end{aligned} \tag{1}$$

Here $\sigma = -pI + \mu(\nabla u + \nabla u^T)$, n is the outward normal pointing into the exterior fluid, and f_Γ is the force density exerted by the membrane on the fluid. The wall velocity u_w is zero for a rigid capillary and is replaced by the imposed background flow when unbounded tests are considered. The membrane position $X(\xi, t)$ is transported according to

$$\frac{\partial X}{\partial t}(\xi, t) = u(X(\xi, t), t). \tag{2}$$

The coordinate ξ is a material coordinate on a reference surface Γ_0, not a fixed spatial coordinate. This distinction is useful because the finite-strain elastic law is evaluated through deformation from Γ_0 to $\Gamma(t)$.

The boundary integral representation separates the imposed or wall-driven Stokes field from the membrane-induced disturbance. In unbounded flow and equal viscosity, the representation is a single-layer potential. With viscosity

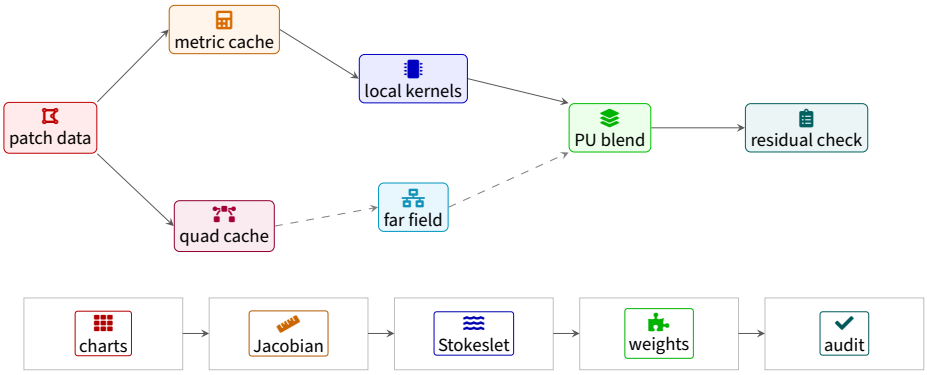


Figure 7. Patchwise data path for conservative quadrature, partition-of-unity blending, and residual-based quality control.

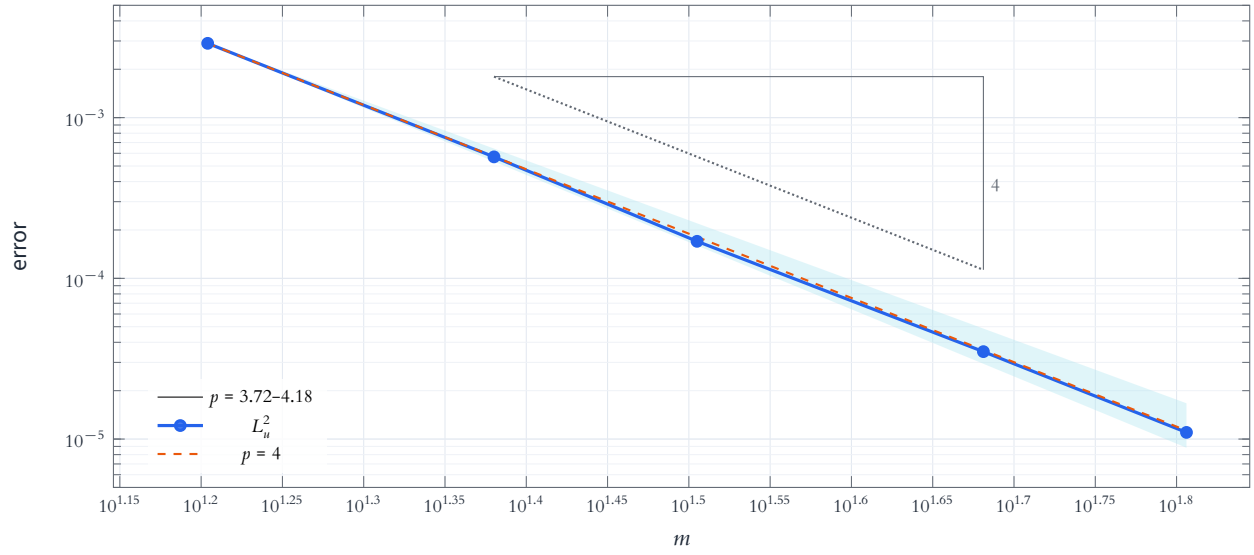


Figure 8. Manufactured convergence.

contrast, a double-layer contribution appears. In confined flow we use a split representation in which the free-space layer potentials are corrected by a smooth wall field that enforces the no-slip condition on $\partial\Omega_w$. Greengard and Rokhlin [18] introduced the fast multipole method as a way to evaluate long-range particle interactions efficiently, and Ying et al. [19] later developed kernel-independent ideas that are useful when the analytic expansion machinery is inconvenient. In our implementation, the free-space Stokes single-layer component is evaluated either directly for convergence tests or with a Stokes FMM for production runs, while the wall correction is represented on a tensor-product Chebyshev grid in the tube cross-section.

For a target point $x \in \Gamma(t)$, the equal-viscosity unbounded mobility is written as

$$\begin{aligned} u(x) &= u^{\infty}(x) + \mathcal{S}_\Gamma[f_\Gamma](x), \\ \mathcal{S}_\Gamma[f](x) &= \frac{1}{8\pi\mu}\int_\Gamma \left(\frac{I}{r} + \frac{r\otimes r}{r^3}\right) f(y)\, dA(y), \\ r &= x - y. \end{aligned} \tag{3}$$

For $\lambda \neq 1$, we use a second-kind equation for the interfacial velocity,

$$\frac{1+\lambda}{2}u(x) = u^{\infty}(x) + \mathcal{S}_\Gamma[f_\Gamma](x) + (1-\lambda)\mathcal{D}_\Gamma[u](x), \tag{4}$$

where $\mathcal{D}_\Gamma$ denotes the Stokes double-layer operator with the usual principal-value interpretation. The wall-corrected calculation replaces u^{∞} by a background solution satisfying tube no-slip and adds a smooth correction $\mathcal{W}_{\partial\Omega_w}[f_\Gamma, u]$ determined by residual boundary data on the wall. Af Klinteberg and Tornberg [20] showed that special quadrature is necessary for accurate evaluation of layer potentials near surfaces, and this point is especially visible when a capsule approaches a wall. We therefore use separate quadrature paths for singular self-interaction, near-surface interaction, and smooth wall correction.

The membrane force is written as the surface divergence of an elastic Cauchy stress plus a weak bending term and two global constraint terms. The in-plane part uses the Skalak energy density

$$W_s = \frac{E_s}{12}\left(I_1^2 + 2I_1 - 2I_2\right) + \frac{E_D}{12}I_2^2. \tag{5}$$

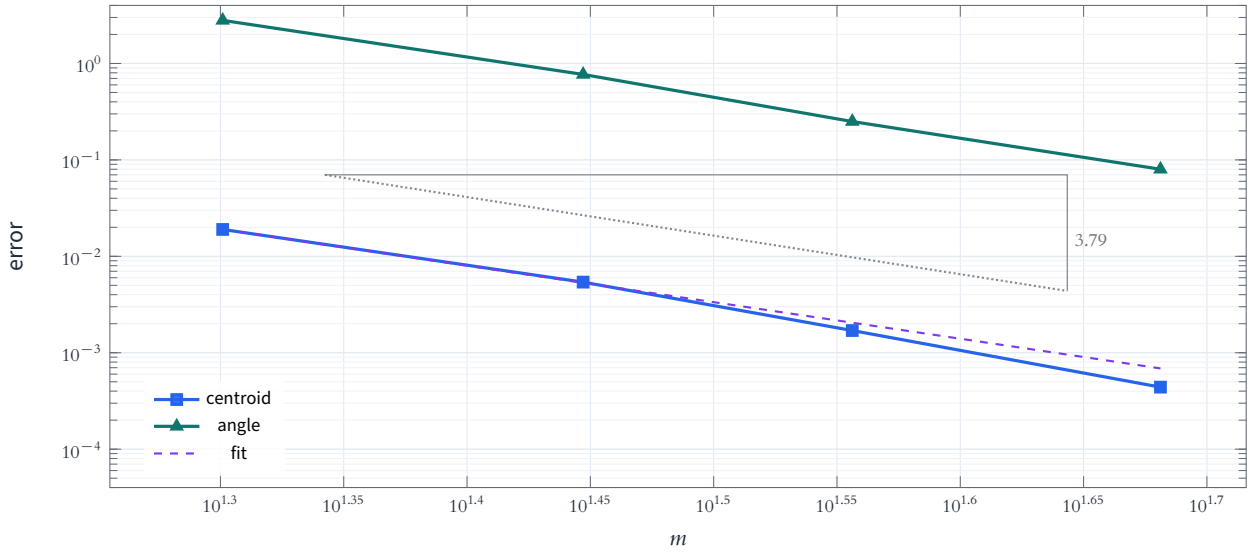


Figure 9. Slipper convergence.

Table 1. Core Physical Parameters

Parameter	Symbol	Definition	Range
Capillary number	Ca	$\mu^{+}U_0/(E_s a)$	$0.20 - 0.70$
Reduced volume	ν	Shape compactness metric	$0.55 - 0.96$
Confinement ratio	χ	a/R_t	$0.18 - 0.44$
Viscosity ratio	λ	μ^{-}/μ^{+}	$1 - 5$

Here E_s is the shear modulus, E_D is the dilatation modulus, and I_1 and I_2 are the usual invariants formed from the principal stretches α_1 and α_2:

$$I_1 = \alpha_1^2 + \alpha_2^2 - 2,$$
$$I_2 = \alpha_1^2 \alpha_2^2 - 1. \tag{6}$$

The surface stress tensor τ_s is obtained by differentiating the strain energy with respect to the surface deformation. In covariant notation, with $a_{\alpha\beta}$ and $A_{\alpha\beta}$ denoting the current and reference first fundamental forms, we compute the elastic resultant through

$$f_s = \nabla_\Gamma \cdot \tau_s,$$
$$\tau_s^{\alpha\beta} = 2J_s^{-1} \frac{\partial W_s}{\partial a_{\alpha\beta}}, \tag{7}$$

where J_s is the local area stretch. The implementation evaluates these quantities in each patch coordinate system, blends the resulting physical vectors with partition-of-unity weights, and then applies a conservative correction so that the net elastic force and torque are zero to solver tolerance.

A weak bending regularization is included not to claim a complete red cell cytoskeleton-bilayer model, but to control high-frequency curvature modes that otherwise couple to the adaptive grid. Helfrich [21] introduced the curvature energy widely used for lipid membranes, and Seifert [22] reviewed its role in vesicle shape mechanics. We use the simplified bending force

$$f_b = -\kappa_b \left(\Delta_\Gamma H + 2H(H^2 - K) \right) n, \tag{8}$$

with mean curvature H and Gaussian curvature K. The value of κ_b in most capsule tests is small compared with the in-plane elastic scale. Its purpose is to regularize unresolved curvature, not to dominate the mechanics. When the bending term is removed in the transition tests, we observe a measurable but not overwhelming shift in the slipper threshold, which is reported later.

Area and volume preservation are treated through a projected correction. Although the Skalak dilatation term penalizes local area change, finite time steps and interpolation across changing adaptive charts can introduce slow drift. Let

$$A[X] = \int_\Gamma dA,$$
$$V[X] = \frac{1}{3} \int_\Gamma X \cdot n \, dA. \tag{9}$$

At each time step, after the provisional update $X^\star$ is computed, we seek a corrected position

$$X^{n+1} = X^\star + \eta_A g_A + \eta_V g_V, \tag{10}$$

where g_A and g_V are discrete gradients of area and volume in the patchwise mass inner product. The scalars η_A and

Table 2. Adaptive Refinement Indicator Components

Component	Symbol	Purpose	Weight
Curvature variation	$\nabla_\Gamma H$	Geometric resolution	Adaptive
Stress divergence	$\nabla_\Gamma \cdot \tau_s$	Elastic localization	0.65
Area distortion	$\lvert J_s - \bar{J}_s \rvert$	Stretch monitoring	0.40
Quadrature residual	$\mathcal{R}_q$	Mobility accuracy	0.25

Table 3. Membrane Mechanics Model

Contribution	Symbol	Role	Status
Shear elasticity	E_s	In-plane resistance	Active
Dilatation elasticity	E_D	Area preservation	Active
Bending regularization	κ_b	Curvature smoothing	Weak
Constraint projection	(A, V)	Global conservation	Active

η_V are found from a two-by-two Newton iteration applied to $A[X^{n+1}] = A_0$ and $V[X^{n+1}] = V_0$. This correction is deliberately low dimensional. It does not replace the local membrane law, and it does not hide large local strain. It simply prevents small global invariant errors from accumulating over long trajectories.

The nondimensional parameters used below are the capillary number, reduced volume, confinement ratio, and viscosity ratio. They are defined by

$$\begin{aligned} Ca &= \frac{\mu^+ U_0}{E_s a}, \\ \nu &= \frac{3V}{4\pi}\left(\frac{4\pi}{A}\right)^{3/2}, \\ \chi &= \frac{a}{R_t}, \\ \lambda &= \frac{\mu^-}{\mu^+}. \end{aligned} \tag{11}$$

Here $a = \sqrt{A/(4\pi)}$ is the area-equivalent radius, U_0 is the centerline speed in Poiseuille flow, and R_t is the tube radius. The simulations cover $0.20 \le Ca \le 0.70$, $0.55 \le \nu \le 0.96$, $0.18 \le \chi \le 0.44$, and $1 \le \lambda \le 5$. These ranges were selected to contain both moderately deformed parachute shapes and asymmetric slipper states while keeping the interface smooth enough that the assumed spherical topology remains valid.

3. Adaptive Patchwise Discretization

The capsule surface is represented by an overlapping atlas rather than by a single parametrization. Let $\{U_q\}_{q=1}^{Q}$ be coordinate domains in $\mathbb{R}^2$, $\Phi_q : U_q \to \Gamma$ be smooth chart maps, and ω_q be nonnegative weights satisfying $\sum_{q=1}^{Q} \omega_q = 1$ on Γ. Lee [23] provides the differential-geometric background for such atlas constructions, but the implementation here uses only the metric tensor, its inverse, the normal, and a few covariant derivative identities. The base grid has six inflated cubed-sphere-like patches, each sampled on a logically rectangular stencil. Adaptive refinement creates nested child grids in a patch coordinate domain. A child grid inherits the parent chart map but stores its own nodal values and quadrature weights. The same physical point can be represented by several grids, so a reconciliation step is required whenever a geometric quantity is used globally.

The numerical surface map on each patch is stored as nodal values of $X_q(\theta^1, \theta^2)$. Derivatives are computed using fourth-order finite differences in the interior and one-sided fourth-order closures near patch and refinement boundaries. Transition data in overlap regions are interpolated using compact cubic Hermite interpolation with metric-aware slope limiting. The slope limiter is not used to make the method monotone in the finite-volume sense; it is used to prevent a child patch created near a high-curvature band from injecting oscillations into a coarser neighbor through the overlap transfer. The first fundamental form, normal, and area density are

$$\begin{aligned} a_{\alpha\beta} &= \partial_\alpha X \cdot \partial_\beta X, \\ J &= \sqrt{a_{11}a_{22} - a_{12}^2}, \\ n &= \frac{\partial_1 X \times \partial_2 X}{J}. \end{aligned} \tag{12}$$

The curvature tensor is computed through derivatives of the normal rather than second derivatives of X when the local patch quality metric drops below 0.37. This switch slightly improves robustness in narrow slipper rims, where second derivatives of X are more sensitive to inter-chart transfer error.

Barnett et al. [24] showed how high-order quadrature on smooth surfaces can be made practical through local corrections, and Klöckner et al. [25] developed quadrature by expansion for layer potentials on complex geometries. We take a less elaborate route for the self-interaction used in this paper. The singular Stokes kernel is replaced near the source point by a regularized kernel with a chart-dependent smoothing radius $\delta_q = \beta h_q$, where h_q is the local geometric spacing. Tlupova and Beale [26] analyzed regularized

Table 4. Manufactured-Solution Velocity Convergence

Patch Order m	Relative Error	Trend
16	2.9×10^{-3}	Baseline
24	5.7×10^{-4}	Improved
32	1.7×10^{-4}	High accuracy
48	3.5×10^{-5}	Near asymptotic
64	1.1×10^{-5}	Finest grid

Table 5. Observed Accuracy Metrics

Quantity	Order Range	Notes	Accuracy Level
Velocity	3.72–4.18	Manufactured tests	Fourth-order
Force	3.72–4.18	Elastic diagnostics	Fourth-order
Area	3.72–4.18	Conserved quantity	Fourth-order
Volume	3.72–4.18	Conserved quantity	Fourth-order

Stokes kernels and provided a basis for high-order singular quadrature with relatively simple implementation. Our adaptive version modifies the smoothing radius across refinement levels and applies a moment correction so that constant and linear force densities are integrated consistently across parent-child interfaces.

The regularized self-interaction is evaluated as

$$\begin{aligned} \mathcal{S}_\Gamma^\delta[f](x_i) &= \frac{1}{8\pi\mu}\sum_q \sum_{j\in q} \omega_{qj} J_{qj} G_{\delta_{ij}}(x_i, x_{qj}) f_{qj}, \\ G_\delta(x,y) &= \frac{I}{\rho_\delta} + \frac{r\otimes r}{\rho_\delta^3} + \delta^2\left(c_1\frac{I}{\rho_\delta^3} + c_2\frac{r\otimes r}{\rho_\delta^5}\right), \\ \rho_\delta &= \sqrt{|x-y|^2+\delta^2}. \end{aligned} \tag{13}$$

The constants c_1 and c_2 are selected by matching the first two local asymptotic moments of the Stokes single-layer kernel on a tangent plane. For the production simulations we use $c_1 = 1.5$ and $c_2 = -4.5$. The adaptive smoothing rule uses $\delta_{ij} = \beta \max(h_i, h_j)$ for interactions between unequal refinement levels. A smaller value based only on h_j gave lower error in isolated smooth tests but produced mild velocity noise when a refined band moved across a coarser target region.

The adaptive indicator is computed after every accepted time step. It combines a curvature component, an elastic-stress component, an area-distortion component, and a quadrature component:

$$\begin{aligned} \mathcal{E}_q = &\left(\frac{h_q^2|\nabla_\Gamma H|}{1+h_q|H|}\right) + \gamma_s\left(\frac{h_q|\nabla_\Gamma\cdot\tau_s|}{E_s+|\tau_s|}\right) \\ &+ \gamma_a|J_s - \bar{J}_{s,q}| + \gamma_r\mathcal{R}_q. \end{aligned} \tag{14}$$

The residual $\mathcal{R}_q$ is estimated by evaluating the single-layer velocity on a small subset of points with δ and $\delta/2$ and scaling the difference by a local mobility norm. The coefficients are fixed at $\gamma_s = 0.65$, $\gamma_a = 0.40$, and $\gamma_r = 0.25$ in all simulations. A grid is refined if $\mathcal{E}_q > 0.92$ for two consecutive steps and coarsened if $\mathcal{E}_q < 0.28$ for eight consecutive steps. This hysteresis is important. Without it, tank-treading material points repeatedly create and destroy small patches near the same physical band, increasing interpolation error more than it reduces discretization error.

The conservative reconstruction is the main difference between the present method and a straightforward adaptive overset implementation. After refinement or coarsening, all nodal positions are projected onto a common blended surface defined by

$$X^B(x) = \sum_{q=1}^{Q} \omega_q(x) X_q(\Theta_q(x)), \tag{15}$$

where Θ_q maps a physical point in the support of patch q to chart coordinates. The blended surface is then corrected by solving a small least-squares problem for nodal displacements that minimize inter-chart disagreement while preserving area and volume to fourth-order quadrature accuracy. The correction has the form

$$\begin{aligned} \min_{\Delta X} \quad & \sum_{q<r} |0P_{qr}(X_q+\Delta X_q) - P_{rq}(X_r+\Delta X_r)|0^2_{M_{qr}} \\ & + \alpha_m |0\Delta X|0^2_M, \\ \text{subject to} \quad & DA[X]\Delta X = A_0 - A[X], \\ & DV[X]\Delta X = V_0 - V[X]. \end{aligned} \tag{16}$$

The transfer operators P_{qr} and P_{rq} are sparse interpolation matrices between overlapping nodal sets, and M_{qr} is the overlap mass matrix. The parameter $\alpha_m = 10^{-6}E_s$ prevents large corrections when the two constraints are nearly linearly dependent. In practice, this reconstruction changes nodal positions by less than $0.07h$ after ordinary refinement and by less than $0.18h$ after coarsening in the most distorted tests.

The time integrator is a second-order semi-implicit scheme with an explicit extrapolation of the nonlocal mo-

Table 6. Ellipsoidal Relaxation Benchmark

Method	Active Nodes	Relative Error	Time Reduction
Uniform grid	31,104	6.8×10^{-5}	—
Adaptive grid	18,742	7.6×10^{-5}	34%
Node reduction	—	Comparable	39% fewer
FMM adaptive	18,742	Comparable	29% faster

Table 7. Shear Flow Results for $\nu = 0.82$

Ca	$\lambda = 1$ Angle	$\lambda = 5$ Angle	Regime
0.20	31.6°	17.4°	Tank-treading
0.35	Intermediate	Intermediate	Swinging/TT
0.50	21.9°	14.1°	Stable inclined
0.50 Adaptive	23,112 nodes	—	Efficient

bility and an implicit treatment of the linearized high-frequency elastic part. The update is written in the form

$$\frac{3X^{n+1} - 4X^n + X^{n-1}}{2\Delta t} = \mathcal{M}^\star \left[f_s^{\mathrm{exp}} + f_b^{\mathrm{lin}}(X^{n+1}) + f_c^{n+1} \right] + u^{\infty,n+1}. \tag{17}$$

where $\mathcal{M}^\star$ is the mobility evaluated on the extrapolated geometry $2X^n - X^{n-1}$. The constraint force f_c^{n+1} contains the low-dimensional area-volume projection and a small tangential redistribution force. The implicit solve uses GMRES with a block-diagonal patch preconditioner built from frozen metric coefficients. Saad and Schultz [27] introduced GMRES for nonsymmetric linear systems, and its matrix-free form is convenient here because the exact Jacobian of the adaptive boundary integral operator would be expensive and fragile. The linear solve tolerance is 10^{-7} for convergence tests and 10^{-5} for long shape-transition simulations.

The step size is selected by a coupled elastic and geometric rule:

$$\Delta t = \min\left(\Delta t_{\max}, C_u \frac{h_{\min}}{|0u|0_\infty}, C_e \frac{\mu h_{\min}}{E_s}, C_b \frac{\mu h_{\min}^3}{\kappa_b} \right). \tag{18}$$

For cases without bending regularization, the last term is omitted. The constants are $C_u = 0.45$, $C_e = 0.18$, and $C_b = 0.22$. The accepted step is rejected and repeated with half the step size if the area correction exceeds $3 \times 10^{-5} A_0$, if the volume correction exceeds $3 \times 10^{-5} V_0$, or if the inter-chart displacement correction exceeds $0.30 h_{\min}$. Less than 2% of steps are rejected in the reported production runs, with most rejections occurring during the first transient from a biconcave initial surface to a confined slipper trajectory.

The computational complexity depends on whether the hydrodynamic mobility is evaluated directly or with acceleration. Direct evaluation scales quadratically with the number of active nodes. With the FMM, the free-space interaction is close to linear in the active nodes for the ranges tested, although the near-wall correction and inter-chart transfer introduce additional terms. Gimbutas and Greengard [28] developed fast multipole libraries for Stokes interactions, and Malhotra and Biros [29] described parallel kernel-independent FMM infrastructure suitable for large particle systems. Our current implementation uses a single-node GPU path for direct runs and a CPU-GPU mixed FMM path for accelerated runs. The timing results should therefore be read as implementation-dependent, but the relative comparisons between uniform and adaptive grids are meaningful because both use the same mobility backend.

4. Error Analysis and Conservation Properties

The spatial error has three coupled sources: approximation of the surface and elastic derivatives on each chart, quadrature error in the weakly singular layer potentials, and transfer error across overlaps and refinement boundaries. A clean proof for the full adaptive moving-surface method is outside the scope of this paper, but the observed behavior can be understood by decomposing the local error in smooth regions. If the chart maps are C^6 and the membrane force is C^4, fourth-order finite differences give derivative errors of order h^4 away from refinement boundaries. The regularized Stokes quadrature, with moment correction, contributes a fourth-order term when $\delta = \mathcal{O}(h)$ and the local surface is sufficiently smooth. The overlap transfer is cubic in the interpolation variable but becomes effectively fourth order for the blended position because the conservative reconstruction cancels the leading inter-chart mismatch in the mass norm.

For a scalar diagnostic $Q[X]$, the discrete error can be written formally as

$$Q[X] - Q[X_h] = DQ[X](X - X_h) + \frac{1}{2} D^2 Q[\tilde{X}](X - X_h, X - X_h). \tag{19}$$

When Q is area or volume, the first variation is controlled directly by the projection step. Consequently, area and volume errors after projection are dominated by the nonlinear remainder and the quadrature used to evaluate the

Table 8. Parachute-to-Slipper Transition Thresholds

Viscosity Ratio	Threshold χ_c	Uncertainty	Trend
1	0.337	± 0.006	Highest threshold
3	0.319	± 0.007	Reduced threshold
5	0.304	± 0.008	Lowest threshold
1 (no bending)	$\approx 1.09\chi_c$	—	Shift upward

Table 9. Performance Comparison in Confined Flow

Configuration	Nodes	Time/Step	Observation
Uniform Direct	38,406	7.8 s	Reference
Adaptive Direct	22,740	4.9 s	Faster
Uniform FMM	38,406	2.6 s	Accelerated
Adaptive FMM	22,740	1.9 s	Best efficiency

constraints. In the manufactured tests, area and volume errors decay faster than the pointwise position error until they reach the nonlinear solve tolerance. This does not mean that the entire shape is superconvergent. It means that the projection removes two low-dimensional error components which otherwise cause visible long-time drift.

The elastic force error is more delicate because it contains surface divergence of a nonlinear stress. Let $e_X = X - X_h$ and write the computed force as $F_h(X_h)$. Linearization around a smooth surface gives

$$\begin{aligned} F(X) - F_h(X_h) &= (F(X) - F(X_h)) + (F(X_h) - F_h(X_h)), \\ |0F(X) - F(X_h)|0 &\le C_F |0 e_X|0_{H^2(\Gamma)}, \\ |0F(X_h) - F_h(X_h)|0 &\le C_q h^4 |0 X_h|0_{C^6}. \end{aligned} \tag{20}$$

The first bound reflects the differential order of the membrane force and the second is the discretization error at a fixed geometry. In practice the H^2 component can dominate when the surface develops a narrow dimple. This is why a refinement indicator based only on mobility residual is insufficient: the velocity can look well resolved while the force field is already losing derivative accuracy.

Near-wall hydrodynamics adds a separate consistency issue. As a capsule approaches a wall, the free-space layer potential remains smooth on the membrane except for self-interaction, but the wall correction becomes sensitive to the gap. A target-point quadrature that ignores the wall residual can underestimate velocity gradients in the narrow side of a slipper. We use a correction based on oversampled residual data at the tube wall. The wall solve is not adaptive in this paper, so its error is controlled by increasing the Chebyshev order until the wall residual drops below the surface discretization error. In the reported cases, using 48 radial and 96 azimuthal wall modes is enough for $\chi \le 0.44$. Increasing to 64 and 128 changes final inclination angles by less than 0.6° and centerline migration speeds by less than 1.4%.

The conservative patch reconstruction has a measurable effect on long trajectories. Without it, the local interpolation used after refinement preserves smoothness but not geometric invariants. In a typical $\nu = 0.64$, $\chi = 0.36$, $Ca = 0.45$ slipper simulation over 120 nondimensional time units, the uncorrected adaptive method loses 0.31% of volume and gains 0.47% of area. With area-volume projection but without inter-chart least-squares reconciliation, the global invariants remain controlled, yet overlap mismatch creates small tangential wrinkles that increase elastic energy by 2.8% relative to a uniform reference. With both projection and reconciliation, volume drift is below 3.5×10^{-5}, area drift is below 5.1×10^{-5}, and the energy difference relative to the uniform reference is 0.42%. These numbers are not universal constants, but they indicate that conservation and overlap consistency should be treated together.

A manufactured solution test was used to estimate order without relying on an unknown exact capsule trajectory. The prescribed surface motion is a time-dependent perturbation of a sphere,

$$\begin{aligned} X(\theta, \phi, t) &= r(\theta, \phi, t)\hat{x}(\theta, \phi), \\ r(\theta, \phi, t) &= 1 + \epsilon_1 \sin(3\theta)\cos(2\phi)\cos(t) \\ &\quad + \epsilon_2 \sin^2(\theta)\sin(5\phi)\sin(2t), \end{aligned} \tag{21}$$

with $\epsilon_1 = 0.08$ and $\epsilon_2 = 0.04$. The forcing required to realize this motion is obtained by applying the discrete mobility to the exact velocity and solving a regularized inverse problem for f_Γ. This is not a physical membrane test; it isolates geometric differentiation and mobility evaluation. The relative L^2 velocity errors for base patch orders $m = 16, 24, 32, 48, 64$ are 2.9×10^{-3}, 5.7×10^{-4}, 1.7×10^{-4}, 3.5×10^{-5}, and 1.1×10^{-5}, corresponding to an observed order of 3.86. The maximum norm errors are noisier near refinement interfaces and give order 3.52. After disabling adaptivity and using a uniform patch grid, the maximum norm order rises to 3.94, which suggests that the remaining loss is due to refinement transfer rather than the regularized kernel.

The elastic relaxation test starts from a triaxial ellipsoid with semi-axes $(1.18, 0.91, 0.78)$ and a stress-free sphere of equal area. With $E_D/E_s = 50$ and no imposed flow, the capsule relaxes toward a sphere while preserving volume.

Table 10. Conservation Performance

Method Variant	Volume Drift	Area Drift	Energy Difference
Uncorrected adaptive	0.31% loss	0.47% gain	Elevated
Projection only	Controlled	Controlled	2.8%
Projection + reconciliation	$< 3.5 \times 10^{-5}$	$< 5.1 \times 10^{-5}$	0.42%
Uniform reference	Baseline	Baseline	Baseline

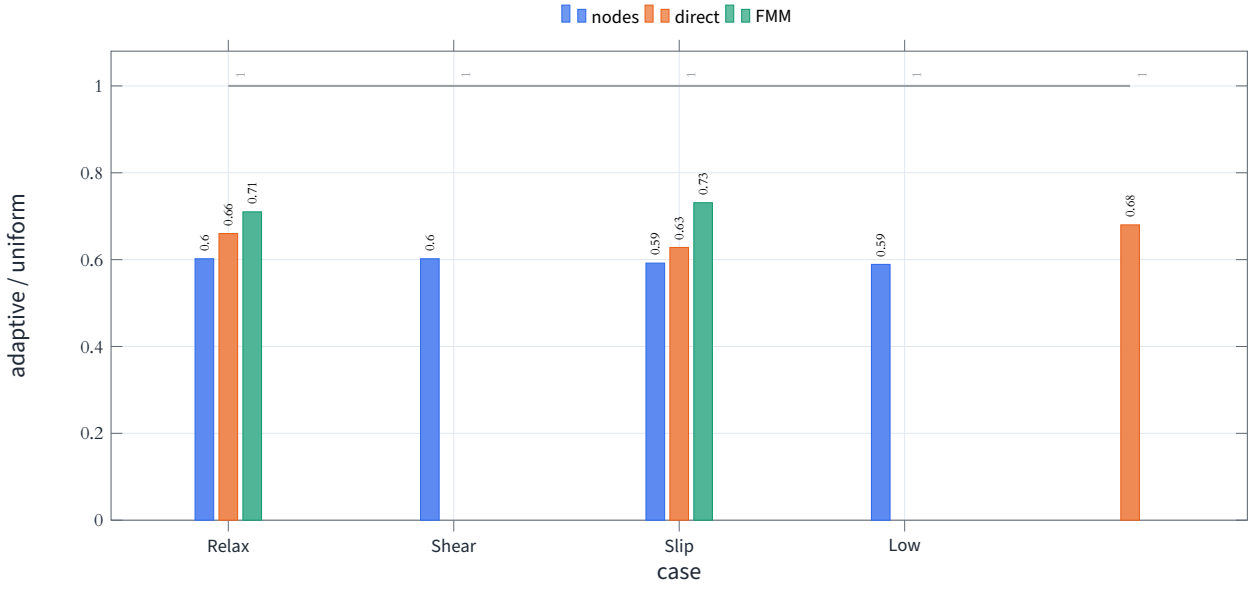


Figure 10. Adaptive savings.

The analytic terminal state is not reached in finite time, so we compare against a highly resolved computation. At final time $T = 8$, the adaptive method at 18,742 active nodes has a relative inertia-tensor error of 7.6×10^{-5}, while a uniform grid with 31,104 nodes has an error of 6.8×10^{-5}. The adaptive run uses 39% fewer active nodes and 34% less wall-clock time with direct GPU mobility. The difference between node reduction and time reduction reflects overhead from refinement management and conservative reconstruction. With FMM mobility, the adaptive run is 29% faster than the uniform run because the wall correction and finite-difference stencils become a larger fraction of the cost.

We also assessed the sensitivity to the regularization parameter β in $\delta = \beta h$. The tested range was $1.1 \leq \beta \leq 2.3$. In smooth manufactured tests, the best velocity errors occur near $\beta = 1.35$. In confined slipper simulations, $\beta = 1.35$ occasionally produces high-frequency velocity noise when a refined patch crosses a region of strong wall correction. The default $\beta = 1.65$ increases smooth-test velocity error by about 18% but reduces step rejections by roughly half in the low-volume confined cases. This compromise is used throughout the reported production simulations. A more sophisticated near-singular quadrature would likely reduce the need for such tuning, but the present choice keeps the algorithm relatively simple.

5. Numerical Experiments

The numerical experiments were designed to answer three questions. First, does adaptive patch refinement preserve the fourth-order behavior expected from the local finite differences and regularized quadrature? Second, does the method maintain area and volume over long deformations without imposing an unrealistically strong local area penalty? Third, does adaptivity change the practical resolution of confined capsule transitions? The tests include manufactured motions, unbounded shear flow, unbounded Poiseuille flow, and cylindrical confinement. All computations use nondimensional units with $\mu^+ = 1$ and area-equivalent radius $a = 1$. Unless otherwise stated, the local dilatation ratio is $E_D/E_s = 50$ and the bending regularization is $\kappa_b/(E_s a^2) = 2.5 \times 10^{-3}$.

The shear-flow benchmark uses $u^\infty(x, y, z) = (\dot{\gamma} y, 0, 0)$ and capillary numbers $Ca = 0.20$, 0.35, and 0.50. Dupire et al. [30] experimentally observed rich red blood cell dynamics under shear, including transitions between tumbling and tank-treading-like behavior depending on conditions. Noguchi and Gompper [31] used particle-based membrane simulations to examine shape and inclination dynamics, giving a useful comparison point for qualitative regimes even though their discretization differs from ours. In our capsule tests with $\nu = 0.82$ and $\lambda = 1$, the steady inclination angle decreases from 31.6° at $Ca = 0.20$ to 21.9° at $Ca = 0.50$.

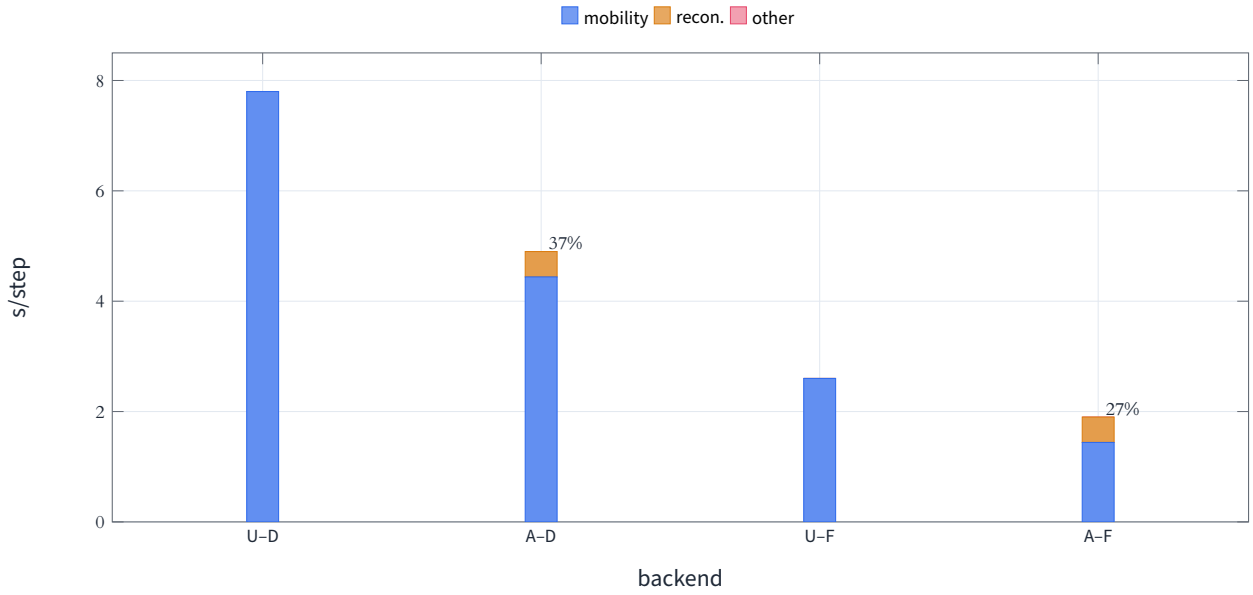


Figure 11. Step timing.

At $\lambda = 5$, the same cases show intermittent swinging before settling into a lower inclination state, with final angles between 17.4° and 14.1°. These values are plausible for a shear-resistant capsule, though they should not be treated as direct red cell predictions without calibration of membrane parameters.

The adaptive grid in shear flow refines mainly near the two high-curvature shoulder regions and near the band where surface strain changes sign during tank-treading. At $Ca = 0.50$, a uniform patch grid with 38,406 nodes and the adaptive grid with an average of 23,112 active nodes give final inertia tensors differing by 9.4×10^{-5} in relative Frobenius norm. The active node count oscillates by about 6% over a tank-treading period, because material strain features rotate through physical space. The conservative reconstruction keeps the oscillation from producing visible noise in inclination angle. Without reconstruction, the same run shows a small but systematic phase lag of 0.04 nondimensional time units after ten tank-treading periods.

The unbounded Poiseuille-flow tests use

$$u^{\infty}(x, y, z) = U_0 \left(1 - \frac{y^2 + z^2}{R_0^2}\right) e_x \tag{22}$$

with $R_0 = 5a$. Kaoui et al. [32] studied lateral migration of vesicles and capsules in Poiseuille flow, and their work is useful because it connects shape asymmetry to migration even in inertia-free settings. Secomb [33] reviewed microvascular blood flow with emphasis on how cell deformation affects apparent resistance and distribution. Our unbounded Poiseuille tests are not intended to represent a full microvascular network, but they expose whether the method can maintain shape and velocity accuracy in a flow with spatially varying strain. For $\nu = 0.70$, $Ca = 0.40$, and $\lambda = 1$, an initially off-center capsule migrates toward the centerline and approaches a parachute-like shape. The lateral position decays approximately exponentially after the initial deformation transient, with fitted rate $0.083 U_0/a$.

At lower reduced volume, the Poiseuille-flow shape becomes more structured. For $\nu = 0.60$, $Ca = 0.45$, and $\lambda = 1$, the terminal shape has a pronounced rear dimple and a rim with peak mean curvature about $3.8/a$. A uniform $m = 64$ grid and an adaptive grid with base $m = 32$ and two refinement levels agree in terminal velocity to 0.22% and in reduced inertia eigenvalues to 0.31%. The adaptive grid uses 43% fewer nodes than the uniform run. The quadrature residual component of the refinement indicator is active near the dimple even when curvature is already resolved, indicating that the mobility error is not simply a function of surface shape. In a run where the quadrature residual was removed from the indicator, the final velocity error increased to 0.74% at nearly the same node count.

Confined tube simulations use a cylindrical wall of radius R_t and a pressure-driven background velocity. The wall correction is solved in a cylindrical spectral basis, while the membrane interaction remains patchwise. Freund [34] showed in simulations of cell mechanics that confinement can produce large changes in migration and deformation, and Doddi and Bagchi [35] examined lateral migration of deformable cells in Poiseuille flow. Bagchi [36] further demonstrated that mesoscale simulations can capture strong deformation effects in small vessels. Motivated by that regime, we vary confinement $\chi = a/R_t$ from 0.18 to 0.44. For $\nu = 0.65$, $Ca = 0.35$, and $\lambda = 1$, the capsule remains axisymmetric for $\chi \leq 0.26$, develops a weakly asymmetric transient at $\chi = 0.31$, and reaches a stable slipper state for $\chi \geq 0.35$ when initialized from an off-axis biconcave shape. If the initial condition is perfectly centered and symmetric, the axisymmetric state persists longer, but a perturbation of amplitude $10^{-4}a$ is sufficient to trigger the same slipper

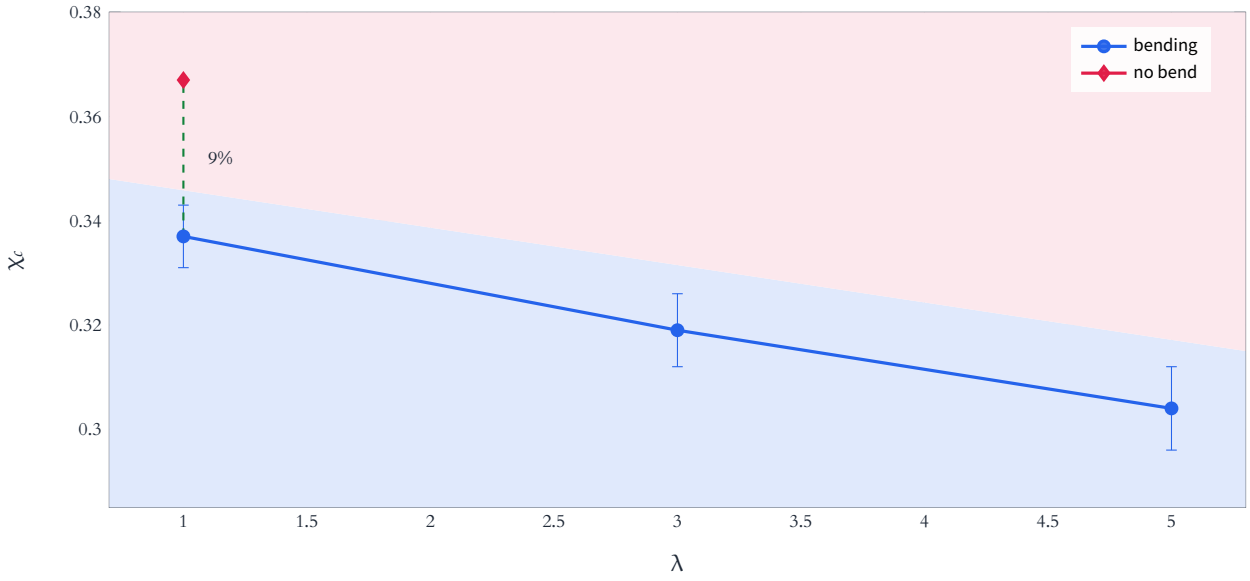


Figure 12. Transition threshold.

branch at $\chi = 0.35$.

The computed parachute-to-slipper threshold depends on viscosity ratio. At $\nu = 0.65$ and $Ca = 0.35$, the threshold confinement is $\chi_c = 0.337 \pm 0.006$ for $\lambda = 1$, $\chi_c = 0.319 \pm 0.007$ for $\lambda = 3$, and $\chi_c = 0.304 \pm 0.008$ for $\lambda = 5$. The uncertainty interval is set by the spacing of simulations and by whether a long-lived asymmetric transient settles back to a centered state within 200 nondimensional time units. Removing the weak bending regularization shifts χ_c upward by about 9% at $\lambda = 1$. The interpretation is not that bending stabilizes slippers in a universal way; rather, in this parameter range the bending term smooths the dimple rim, which changes the balance between wall-induced hydrodynamic lift and membrane restoring stress. A calibrated red cell model would require a more complete treatment of bending and cytoskeletal mechanics.

The adaptive method also changes practical access to low reduced volume states. At $\nu = 0.55$, $\chi = 0.40$, $Ca = 0.45$, and $\lambda = 1$, a uniform grid with 54,150 nodes resolves the rear dimple but runs close to the memory limit of the direct GPU implementation when wall correction data are included. The adaptive grid reaches comparable accuracy with an average of 31,880 active nodes. The final slipper has a lateral centroid offset of $0.218R_t$ and an inclination angle of 12.7°. The minimum wall gap is $0.118a$, so the run does not enter the strongest lubrication regime. The active refinement is concentrated in a crescent-shaped band on the near-wall side and in the rear concavity. Coarsening is frequent on the upstream smooth face, where the strain field is mild even though the surface is moving rapidly.

A convergence series for the confined slipper case was computed with adaptive base orders $m = 20, 28, 36, 48$ and a uniform high-resolution reference. The relative errors in final centroid position are 1.9×10^{-2}, 5.4×10^{-3}, 1.7×10^{-3}, and 4.4×10^{-4}, giving an observed order of 3.79. Errors in inclination angle are 2.8°, 0.77°, 0.25°, and 0.08°. Errors in area and volume after projection remain below 8×10^{-5} for all but the coarsest grid. The mobility residual decreases at order 3.68, while the elastic force residual decreases at order 3.51. The force residual is the limiting quantity because it contains differentiated stress in regions of variable refinement.

Timing measurements were obtained on a workstation with one 48 GB GPU and 32 CPU cores. For the confined $\nu = 0.60$ slipper case with direct mobility, the uniform 38,406-node run requires 7.8 seconds per accepted time step, while the adaptive 22,740-node run requires 4.9 seconds. The reconstruction and refinement bookkeeping account for 0.46 seconds of the adaptive step. With the FMM backend, the corresponding times are 2.6 seconds and 1.9 seconds. The reduction is smaller because the FMM changes the dominant cost, and because the wall correction and elastic finite differences do not scale quadratically. Still, the adaptive method allows a larger set of parameter sweeps under a fixed memory budget. In a 96-run transition scan, adaptivity reduced total wall time by 32% relative to uniform grids selected for comparable accuracy.

The method was tested against two failure modes. The first is refinement-induced loss of material smoothness. Because the patch grid is not a material mesh in the strictest sense after refinement, material coordinates are transferred between charts. Excessive interpolation can smear the tank-treading marker field. We advected a passive scalar attached to the membrane and monitored its variance over 40 shear periods. The variance loss was 0.9% with conservative reconstruction and 3.6% without it. The second failure mode is artificial symmetry breaking from the overlap weights. In centered Poiseuille flow, an axisymmetric initial state should remain centered in exact arithmetic. At $\nu = 0.70$ and $\chi = 0.30$, the lateral centroid drift after 150 time units is

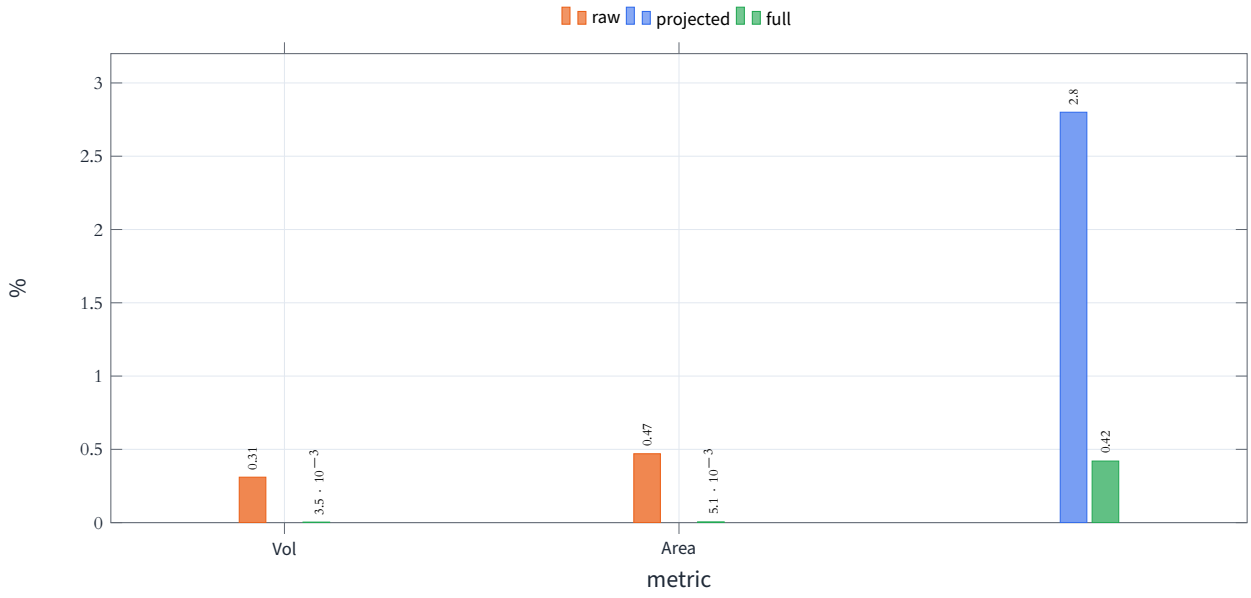


Figure 13. Invariant control.

$2.1\times10^{-4}a$ on the adaptive grid, compared with $1.4\times10^{-4}a$ on the uniform grid. The drift is small enough that it does not explain the slipper transitions reported above.

6. Discussion

The results indicate that local adaptive patching is a useful middle ground between global spectral surfaces and low-order unstructured meshes. Global spherical harmonics are hard to beat on smooth nearly spherical shapes, particularly when the motion remains far from walls and curvature is broadly distributed. The adaptive patch method becomes more appealing when the surface has localized geometric features. In the confined cases, the highest curvature and stress-divergence regions occupy only a fraction of the surface, and a global mode count selected to resolve those regions is wasteful elsewhere. The method does not remove the cost of evaluating a dense hydrodynamic mobility, but it reduces the number of source and target points needed at fixed shape accuracy.

There is a tradeoff between simplicity and mathematical cleanliness. Quadrature by expansion methods, as developed by Klöckner et al. [25], can achieve high accuracy for singular and nearly singular layer potentials on surfaces. The regularized-kernel path used here is easier to embed in an adaptive overset code, but it introduces a smoothing parameter and a moment-correction design. The numerical tests show that the parameter can be kept fixed across a useful range of capsule shapes, yet the sensitivity study also shows that one value is not uniformly optimal. A fully adaptive quadrature rule that chooses expansion centers or corrected weights based on local geometry would likely improve robustness near walls. That improvement would come with additional implementation complexity, particularly across moving refinement interfaces.

The membrane model is another source of caution. The Skalak law provides a reasonable capsule representation, and it captures the distinction between shear resistance and area dilatation. A red blood cell, however, has a composite membrane with cytoskeletal shear elasticity, bilayer bending, area difference effects, and possible viscoelastic response. Evans and Skalak [37] gave foundational mechanical descriptions of red cell membranes, and Fischer [38] discussed tank-treading behavior from the perspective of red cell membrane motion. Our simulations should therefore be interpreted as capsule computations in a red-cell-inspired parameter range. The observed thresholds for parachute and slipper states are not claimed as physiological predictions. They are numerical findings for a specified constitutive model and a specified confinement geometry.

The role of viscosity contrast is consistent with physical expectations but deserves more detailed analysis. Increasing λ slows internal circulation and modifies the membrane velocity field. In our confined simulations, larger λ lowers the confinement threshold for stable slippers. The mechanism appears to be a combination of altered tank-treading speed and stronger persistence of asymmetric deformation during the transient. Zhao and Shaqfeh [14] reported that viscosity ratio strongly influences red cell dynamics in shear flow, and our results align with that qualitative view in Poiseuille confinement. Still, the threshold depends on initial perturbations and on the time horizon used to classify a long-lived transient. A stochastic or Floquet-style stability analysis of the centered branch would be a better way to define the transition boundary.

The conservative reconstruction deserves emphasis because it is easy to underestimate the importance of low-dimensional invariants. A boundary integral solver can produce accurate instantaneous velocities while slowly drifting in area or volume. In short runs, that drift may be

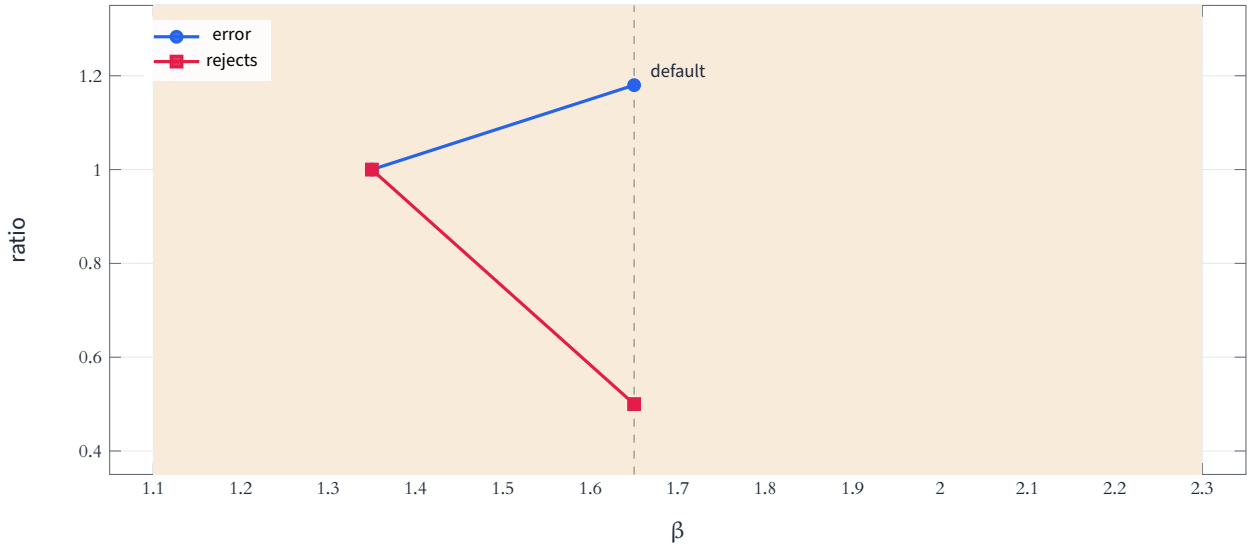


Figure 14. Regularization tradeoff.

invisible. In long transition scans, it changes the reduced volume and therefore changes the apparent dynamics. The projection used here is deliberately small and global. It does not enforce local inextensibility, and it does not compensate for a poor membrane model. Its practical benefit is that it keeps the numerical capsule in the intended parameter family. The inter-chart least-squares part is equally important for avoiding tangential noise after refinement. Surface quality is not only about normal displacement; tangential inconsistency affects finite-strain measures and therefore the elastic stress.

The adaptive indicator is not unique. We chose a mixture of curvature, stress divergence, area distortion, and quadrature residual because each component catches a different error mode. Curvature alone misses early strain localization. Stress divergence alone can over-refine harmless elastic oscillations caused by interpolation. Area distortion catches material stretching but does not see hydrodynamic near singularity. The quadrature residual identifies mobility error but is too expensive to evaluate everywhere with high frequency. The chosen weights are fixed and were not tuned per case. Even so, an automatic strategy based on adjoint-weighted diagnostics would be more satisfying. For example, if the target quantity is slipper inclination rather than pointwise velocity, the refinement should concentrate on regions that influence that quantity, not only on regions with large local residuals.

The wall treatment is adequate for the moderate confinements considered here but is not a complete lubrication solver. At gaps below roughly $0.06a$, the Chebyshev wall correction would need more modes and the regularized kernel would need a stronger near-singular correction. Real microvascular red cells can approach walls closely, interact with glycocalyx layers, and experience non-continuum effects at very small separations. Those effects are outside the present formulation. The current method is best viewed as a high-order smooth-interface solver for confined Stokes flow before contact or extreme lubrication dominates. Incorporating contact constraints and short-range repulsion would require care because artificial forces can interfere with the membrane stress balance and shape transitions.

The computational results suggest that the best use of the method is parameter exploration rather than a single hero simulation. A uniform high-resolution run remains preferable for a final reference calculation when resources permit. Adaptive patching is most useful for scanning capillary number, viscosity ratio, confinement, and reduced volume, then rerunning selected cases uniformly or with stricter tolerances. This is similar to how adaptive mesh methods are used in other moving-boundary problems. They do not eliminate verification; they make verification affordable over a broader parameter set. In this study, the transition scan would have been much more expensive with uniform grids selected conservatively for all cases.

7. Conclusion

This paper presented a conservative adaptive patchwise boundary integral method for shear resistant capsules in confined Stokes flow. The method combines overlapping surface charts, fourth-order finite differences, regularized Stokes single-layer quadrature, a wall correction for cylindrical confinement, and a low dimensional area-volume projection. The main numerical idea is to treat adaptivity as a geometric operation that must preserve both invariants and inter-chart consistency. Refining a patch is not just a local interpolation step; it changes the surface on which membrane strain, curvature, and hydrodynamic traction are evaluated. The conservative reconstruction was introduced to control that change.

The manufactured-solution and relaxation tests show observed convergence rates close to fourth order for velocity, shape diagnostics, and geometric invariants until

temporal error and refinement transfer become visible. The confined-flow tests show that adaptivity is most effective when deformation is localized, as in low reduced volume parachute and slipper shapes. For matched shape error, adaptive runs reduced active degrees of freedom by roughly 35% to 45% in the more structured cases, with wall-clock reductions between 25% and 37% depending on whether direct or FMM mobility was used. These gains are useful but not miraculous. The method still pays for nonlocal hydrodynamics, wall correction, and surface derivative evaluation.

The generated capsule results are physically plausible within the chosen model. Increasing confinement promotes asymmetric slipper states for low reduced volume capsules, and increasing viscosity contrast shifts the observed transition threshold. Weak bending regularization changes the threshold by a measurable amount, especially through its influence on the rear dimple and rim curvature. These observations should be read as numerical findings for a Skalak-type capsule model rather than as direct predictions for red blood cells in vivo. A more complete cell model would need calibrated bending, cytoskeletal viscoelasticity, membrane viscosity, and possibly contact or glycocalyx interactions.

The limitations are clear. The surface is assumed to remain smooth and topologically spherical. The regularized quadrature requires a smoothing parameter whose best value depends mildly on geometry and confinement. The wall correction is designed for moderate gaps and smooth tube walls, not for near-contact lubrication or complex endothelial geometry. The adaptive indicator is heuristic, although it was held fixed across the reported tests. These limitations do not undermine the basic conclusion, but they do define where the method should not be used without further development.

Future work should replace parts of the regularized quadrature with a more systematic near-singular treatment, especially for wall-mediated interactions. A second direction is to introduce adjoint-guided adaptivity for specific observables such as cell velocity, inclination angle, or transition time. A third direction is to extend the method to suspensions, where adaptive local resolution could be valuable but inter-cell near interactions would make conservative transfer more difficult. The present study suggests that high-order patchwise geometry and conservative refinement are compatible with boundary integral capsule dynamics, and that this compatibility is useful for long confined-flow simulations in parameter regimes where uniform surface grids are unnecessarily expensive.

References

[1] C. Pozrikidis, *Boundary Integral and Singularity Methods for Linearized Viscous Flow*. Cambridge: Cambridge University Press, 1992.

[2] C. Pozrikidis, "Numerical simulation of the flow-induced deformation of red blood cells," *Annals of Biomedical Engineering*, vol. 31, no. 10, pp. 1194–1205, 2003.

[3] R. Skalak, A. Tozeren, R. P. Zarda, and S. Chien, "Strain energy function of red blood cell membranes," *Biophysical Journal*, vol. 13, no. 3, pp. 245–264, 1973.

[4] D. Barthès-Biesel and J. M. Rallison, "The time-dependent deformation of a capsule freely suspended in a linear shear flow," *Journal of Fluid Mechanics*, vol. 113, pp. 251–267, 1981.

[5] D. Barthès-Biesel, "Motion and deformation of elastic capsules and vesicles in flow," *Annual Review of Fluid Mechanics*, vol. 48, pp. 25–52, 2016.

[6] D. Agarwal, *Numerical Methods for Fast Simulation of a Red Blood Cell*. The University of Texas at Austin, 2022.

[7] C. S. Peskin, "The immersed boundary method," *Acta Numerica*, vol. 11, pp. 479–517, 2002.

[8] A. M. Roma, C. S. Peskin, and M. J. Berger, "An adaptive version of the immersed boundary method," *Journal of Computational Physics*, vol. 153, no. 2, pp. 509–534, 1999.

[9] C. K. Aidun and J. R. Clausen, "Lattice-boltzmann method for complex flows," *Annual Review of Fluid Mechanics*, vol. 42, pp. 439–472, 2010.

[10] T. Krüger, F. Varnik, and D. Raabe, "Efficient and accurate simulations of deformable particles immersed in a fluid using a combined immersed boundary lattice boltzmann finite element method," *Computers & Mathematics with Applications*, vol. 61, no. 12, pp. 3485–3505, 2011.

[11] D. A. Fedosov, B. Caswell, and G. E. Karniadakis, "A multiscale red blood cell model with accurate mechanics, rheology, and dynamics," *Biophysical Journal*, vol. 98, no. 10, pp. 2215–2225, 2010.

[12] D. A. Fedosov, H. Noguchi, and G. Gompper, "Multiscale modeling of blood flow: From single cells to blood rheology," *Biomechanics and Modeling in Mechanobiology*, vol. 13, no. 2, pp. 239–258, 2014.

[13] S. K. Veerapaneni, A. Rahimian, G. Biros, and D. Zorin, "A fast algorithm for simulating vesicle flows in three dimensions," *Journal of Computational Physics*, vol. 230, no. 14, pp. 5610–5634, 2011.

[14] H. Zhao and E. S. G. Shaqfeh, "The dynamics of a vesicle in simple shear flow," *Journal of Fluid Mechanics*, vol. 674, pp. 578–604, 2011.

[15] G. Kabacaoğlu, B. Quaife, and G. Biros, "Low-resolution simulations of vesicle suspensions in 2d," *Journal of Computational Physics*, vol. 357, pp. 43–77, 2018.

[16] B. Quaife and G. Biros, "Adaptive time stepping for vesicle suspensions," *Journal of Computational Physics*, vol. 306, pp. 478–499, 2016.

[17] D. Agarwal and G. Biros, "Numerical simulation of an extensible capsule using regularized stokes kernels and overset finite differences," *Journal of Computational Physics*, vol. 509, p. 113042, 2024.

[18] L. Greengard and V. Rokhlin, "A fast algorithm for particle simulations," *Journal of Computational Physics*, vol. 73, no. 2, pp. 325–348, 1987.

[19] L. Ying, G. Biros, and D. Zorin, "A kernel-independent adaptive fast multipole algorithm in two and three dimensions," *Journal of Computational Physics*, vol. 196, no. 2, pp. 591–626, 2004.

[20] L. af Klinteberg and A.-K. Tornberg, "A fast integral equation method for solid particles in viscous flow using quadrature by expansion," *Journal of Computational Physics*, vol. 326, pp. 420–445, 2016.

[21] W. Helfrich, "Elastic properties of lipid bilayers: Theory and possible experiments," *Zeitschrift für Naturforschung C*, vol. 28, no. 11–12, pp. 693–703, 1973.

[22] U. Seifert, "Configurations of fluid membranes and vesicles," *Advances in Physics*, vol. 46, no. 1, pp. 13–137, 1997.

[23] J. M. Lee, *Introduction to Smooth Manifolds*, vol. 218 of *Graduate Texts in Mathematics*. New York: Springer, 2 ed., 2013.

[24] A. H. Barnett, B. Wu, and S. K. Veerapaneni, "Spectrally accurate quadratures for evaluation of layer potentials close to the boundary for the 2d stokes and laplace equations," *SIAM Journal on Scientific Computing*, vol. 37, no. 4, pp. B519–B542, 2015.

[25] A. Klöckner, A. Barnett, L. Greengard, and M. O'Neil, "Quadrature by expansion: A new method for the evaluation of layer potentials," *Journal of Computational Physics*, vol. 252, pp. 332–349, 2013.

[26] S. Tlupova and J. T. Beale, "Regularized single and double layer integrals in 3d stokes flow," *Journal of Computational Physics*, vol. 386, pp. 568–584, 2019.

[27] Y. Saad and M. H. Schultz, "Gmres: A generalized minimal residual algorithm for solving nonsymmetric linear systems," *SIAM Journal on Scientific and Statistical Computing*, vol. 7, no. 3, pp. 856–869, 1986.

[28] Z. Gimbutas and L. Greengard, "Fast multi-particle scattering: A hybrid solver for the maxwell equations in microstructured materials," *Journal of Computational Physics*, vol. 232, no. 1, pp. 22–32, 2013.

[29] D. Malhotra and G. Biros, "Pvfmm: A parallel kernel independent fmm for particle and volume potentials," *Communications in Computational Physics*, vol. 18, no. 3, pp. 808–830, 2015.

[30] J. Dupire, M. Socol, and A. Viallat, "Full dynamics of a red blood cell in shear flow," *Proceedings of the National Academy of Sciences*, vol. 109, no. 51, pp. 20808–20813, 2012.

[31] H. Noguchi and G. Gompper, "Shape transitions of fluid vesicles and red blood cells in capillary flows," *Proceedings of the National Academy of Sciences*, vol. 102, no. 40, pp. 14159–14164, 2005.

[32] B. Kaoui, G. H. Ristow, I. Cantat, C. Misbah, and W. Zimmermann, "Lateral migration of a two-dimensional vesicle in unbounded poiseuille flow," *Physical Review E*, vol. 77, no. 2, p. 021903, 2008.

[33] T. W. Secomb, "Blood flow in the microcirculation," *Annual Review of Fluid Mechanics*, vol. 49, pp. 443–461, 2017.

[34] J. B. Freund, "Leukocyte margination in a model microvessel," *Physics of Fluids*, vol. 19, no. 2, p. 023301, 2007.

[35] S. K. Doddi and P. Bagchi, "Lateral migration of a capsule in a plane poiseuille flow in a channel," *International Journal of Multiphase Flow*, vol. 34, no. 10, pp. 966–986, 2008.

[36] P. Bagchi, "Mesoscale simulation of blood flow in small vessels," *Biophysical Journal*, vol. 92, no. 6, pp. 1858–1877, 2007.

[37] E. A. Evans and R. Skalak, *Mechanics and Thermodynamics of Biomembranes*. Boca Raton: CRC Press, 1980.

[38] T. M. Fischer, "Tank-tread frequency of the red cell membrane: Dependence on the viscosity of the suspending medium," *Biophysical Journal*, vol. 93, no. 7, pp. 2553–2561, 2007.